nature astronomy

LETTERS

https://doi.org/10.1038/s41550-020-1156-6

Check for updates

Global helium abundance measurements in the solar corona

John D. Moses[1]✉, Ester Antonucci[2], Jeffrey Newmark[3]✉, Frédéric Auchère[4], Silvano Fineschi[2], Marco Romoli[5], Daniele Telloni[2], Giuseppe Massone[2], Luca Zangrilli[2], Mauro Focardi[6], Federico Landini[6], Maurizio Pancrazzi[5], Guglielmo Rossi[5], Andrea M. Malvezzi[7], Dennis Wang[8], Jean-Christophe Leclec'h[4], Jean-Pierre Moalic[4], Frédéric Rouesnel[4], Lucia Abbo[2], Aurélien Canou[4], Nicolas Barbey[4], Chloé Guennou[4], John M. Laming[8], James Lemen[9], Jean-Pierre Wuelser[9], John L. Kohl[10] and Lawrence D. Gardner[11]

Solar abundances have been historically assumed to be representative of cosmic abundances. However, our knowledge of the solar abundance of helium, the second most abundant element, relies mainly on models[1] and indirect measurements through helioseismic observations[2], because actual measurements of helium in the solar atmosphere are very scarce. Helium cannot be directly measured in the photosphere because of its high first ionization potential, and measurements of its abundance in the inner corona have been sporadic[3,4]. In this Letter, we present simultaneous global images of the helium (out to a heliocentric distance of $3R_\odot$ (solar radii)) and hydrogen emission in the solar corona during the minimum of solar activity of cycle 23 and directly derive the helium abundance in the streamer region and surrounding corona (out to $2.2R_\odot$). The morphology of the He^+ corona is markedly different from that of the H corona, owing to significant spatial variations in helium abundance. The observations show that the helium abundance is shaped according to and modulated by the structure of the large-scale coronal magnetic field and that helium is almost completely depleted in the equatorial regions during the quiet Sun. This measurement provides a trace back to the coronal source of the anomalously slow solar wind observed in the heliosphere at the Sun–Earth Lagrangian point L1 in 2009, during the exceptionally long-lasting minimum of solar activity cycle 23.

The Helium Resonance Scattering in the Corona and Heliosphere (HERSCHEL) sounding rocket investigation obtained simultaneous global images of the He and H solar corona out to 3 solar radii ($3R_\odot$). From these images, we detected helium resonant scattering over a wide region of the corona, and we derived the He abundance map in the region where the acceleration of the solar wind is expected to occur. As helium is the largest contributor to the density of coronal plasma after hydrogen, and as it is four times heavier than hydrogen, helium has a significant influence on the dynamics and mass flux of the solar wind[5–7]. Measurement of the helium abundance is necessary to fully understand the mechanisms responsible for the origin and acceleration of the wind.

The HERSCHEL sounding rocket payload was launched on 14 September 2009 from the White Sands Missile Range, New Mexico, at 16 : 40 UT, and achieved 397.4 s of observations. A joint observational programme was conducted with three instruments on the Solar and Heliospheric Observatory (SOHO): the Extreme ultraviolet Imaging Telescope (EIT), the Large Angle and Spectrometric Coronagraph (LASCO) and the Ultraviolet Coronagraph Spectrometer (UVCS). The HERSCHEL instrument package was composed of the Sounding-rocket Coronagraph Experiment (SCORE), the Helium Coronagraph (HECOR) and the HERSCHEL Extreme Ultraviolet Imaging Telescope (HEIT). SCORE is an externally occulted coronagraph that obtains simultaneous narrow-band H I 121.6 nm, He II 30.4 nm and visible light images of the inner region of the corona (the K-corona) from $1.5R_\odot$ to $2.2R_\odot$(refs. [8,9], S.F., manuscript in preparation). HECOR is a high-throughput, externally occulted coronagraph that obtains narrow-band He II 30.4 nm images from $1.3R_\odot$ to $3R_\odot$ (ref. [10]). HEIT is derived from an engineering model of the Extreme UltraViolet Imager on the Solar Terrestrial Relations Observatory (STEREO)[11] and measures the intensity of the 30.4 nm He II disk emission.

The H I and He II images obtained with SCORE over the west half of the solar corona show markedly different morphologies (Fig. 1a,b). The H I emission is roughly uniform throughout the region across the equator, whereas the He II emission, dimmed in the equatorial region, shows a more complex structure (Fig. 1c), similar to that of the green corona (Fe XIV 530.3 nm) pattern observed during low solar activity in the previous cycle[12]. The difference between the H and He coronal configuration also is reminiscent of that seen in previous observations made with UVCS on SOHO: H I Lyman α (Lyα) and O VI images of quiescent streamers had strikingly different structures, with the oxygen emission in the latter characterized by core dimming[13] in the central region of the streamer belt. As expected, little emission is present in either line over the polar coronal holes where the plasma has both a low density and a high radial velocity. There is a very good match between the morphologies shown in the He II images obtained from SCORE and HECOR

[1]National Aeronautics and Space Administration (NASA), Washington, DC, USA. [2]National Institute for Astrophysics (INAF), Astrophysical Observatory of Torino, Pino Torinese, Italy. [3]National Aeronautics and Space Administration (NASA), Greenbelt, MD, USA. [4]Institut d'Astrophysique Spatiale (IAS), Université Paris-Sud, CNRS, Orsay, France. [5]Università di Firenze, Firenze, Italy. [6]National Institute for Astrophysics (INAF) Astrophysical Observatory of Arcetri, Firenze, Italy. [7]Università di Pavia, Pavia, Italy. [8]Space Science Division, Naval Research Laboratory (NRL), Washington, DC, USA. [9]Lockheed Martin Solar and Astrophysics Laboratory (LMSAL), Palo Alto, CA, USA. [10]Harvard Smithsdonisan Center for Astrophysics, Cambridge, MA, USA. [11]Space Systems Research Corporation (SSRC), Alexandria, VA, USA. ✉e-mail: dan.moses@nasa.gov; jeffrey.newmark@nasa.gov

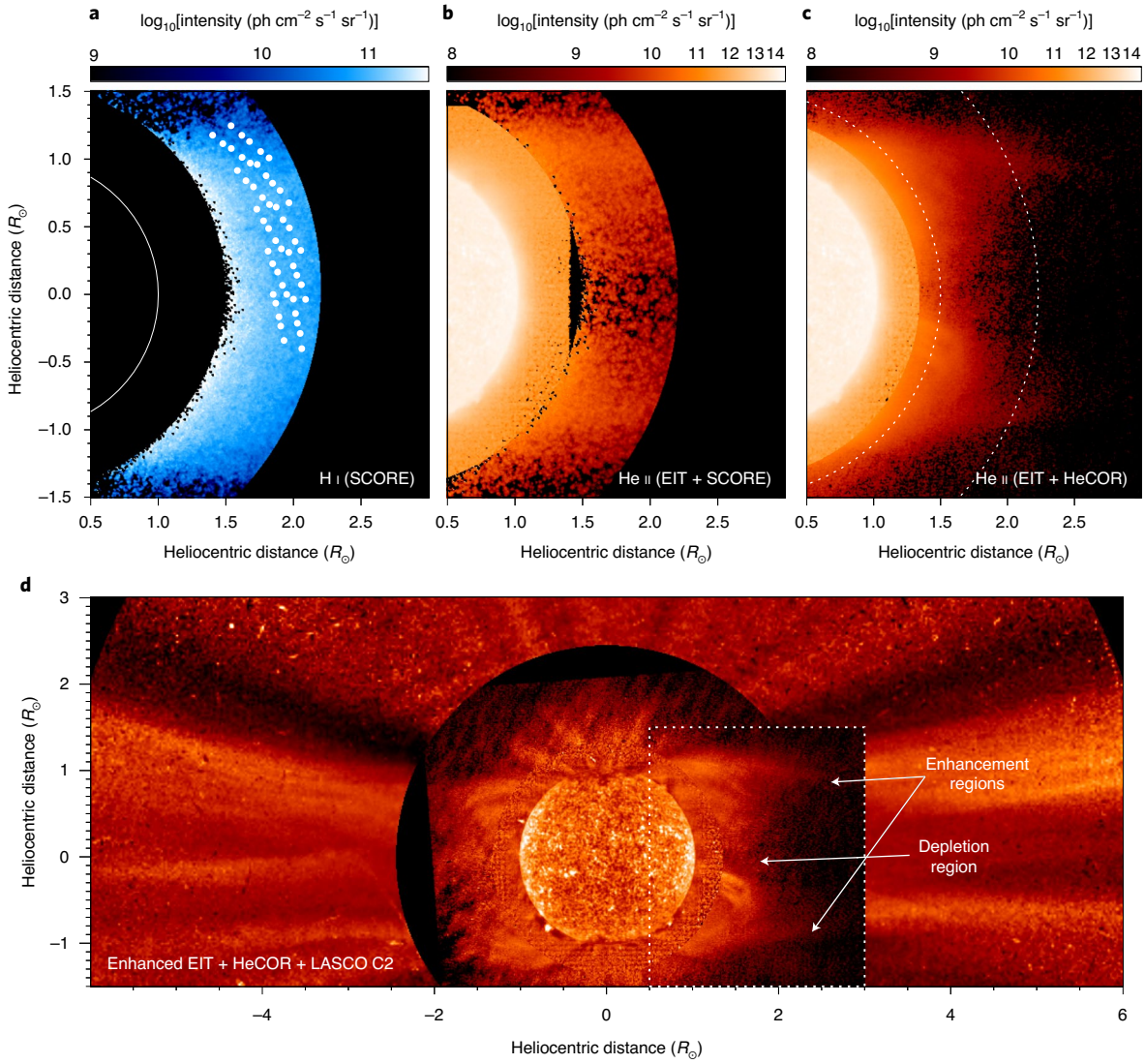

Fig. 1 | Global images of He II emission in the solar atmosphere out to $3R_\odot$ in the frame of the visible light polarized emission of the corona out to $6R_\odot$. **a**,**b**, The photometric images obtained in the SCORE H I Lyα (**a**) and He II channels (**b**) from 1.5 to $2.2R_\odot$. The white dots in **a** indicate the location of the co-ordinated SOHO UVCS observations. **c**, The photometric image obtained in the HECOR He II channel from 1.28 to $3R_\odot$. The stray light-corrected photometric image from the EIT He II channel is included inside the He II channel coronagraph images in **b** and **c**. **d**, An illustration of the global morphology on 14 September 2009, achieved by applying a radial filter (smoothed over 20° polar angle segments) to a composite image consisting of the EIT He II channel inside $1.28R_\odot$, the HECOR He II channel from 1.28 to $2.3R_\odot$ and the LASCO C2 polarized brightness (pB) image at greater coronal heights. The box outlined by the dotted lines in **d** indicates the fields of view of **a**–**c** and that of Fig. 3.

(Fig. 1c) (although these instruments have slightly different passbands centred on the He II 30.4 nm line), and also between those of the westernmost extensions of HECOR and the LASCO C2 image (Fig. 1d). This indicates that the unique structures observed in He II are neither instrumental nor nearby line contamination artefacts.

The helium coronal abundance, given as the ratio of the number of He atoms to H atoms, is derived from the H I and He II line intensity ratio as described in Methods. The polar profiles of the He abundance are plotted in Fig. 2 for three different altitudes: 1.7, 1.9 and $2.1R_\odot$. Extremely low abundance values (≤3%) are observed within ±15° across the equator at the west limb, with a minimum value (0.6%) close to the equator. The increase in He abundance with distance from the equatorial region is more clearly observed in the northern hemisphere, which corresponds to higher latitude degrees. The He abundances near the equator are well below 4.8%, the value measured at $1.5R_\odot$ in the central region of a quiescent equatorial streamer during the solar minimum of cycle 22, from a UVCS observation of the He II 108.5 nm Balmer line[14]. Figure 3 shows the He abundance values superposed on the He II EIT and HECOR composite image. Also shown are the magnetic field lines extrapolated from the photospheric magnetic field using the force-free potential approximation. The centre of the region of the lowest He abundance observed with SCORE falls in between the two closed loop systems that characterize the inner corona below $1.7–1.8R_\odot$. Outside the latitude range ±15° and beyond $1.7R_\odot$, where the magnetic field lines are predominantly open towards interplanetary space (Fig. 3), the He abundance increases but remains less than 10%, a limit that is close to the abundance in the outer convection zone[15]. In Fig. 2, the He abundance is shown for the latitude ranges in which this quantity is only marginally affected by the coronal outflows that cause the H and He emission lines to dim[16]. The coronal He abundances match in situ He abundances of the solar wind as measured at the

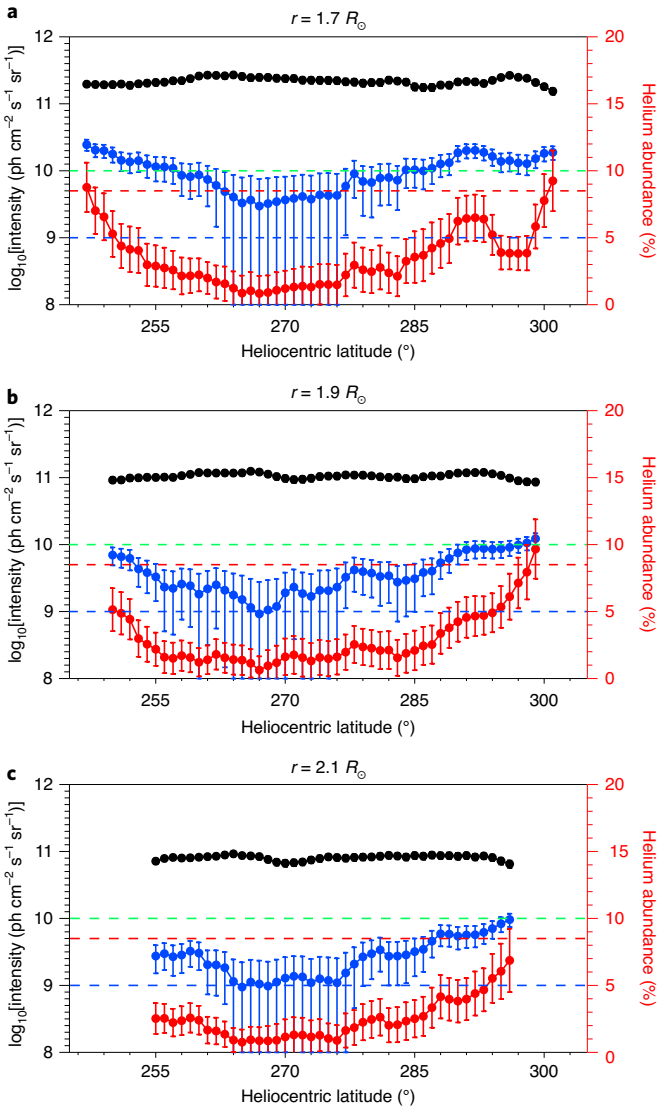

Fig. 2 | Polar profiles of the He abundance. a–c, Polar profiles of coronal He abundances at the west solar limb, as derived from SCORE measurements at 1.7 (**a**), 1.9 (**b**) and 2.1 (**c**) solar radii above the Sun's surface. The heliocentric latitude is expressed in degrees, counter-clockwise from the north pole. The helium abundance (red dots) is compared with the H I and He II intensities (black and blue dots, respectively). The error bars (smaller than the symbols for the H I intensity) refer to 1σ (s.d.) uncertainties. The horizontal dashed lines represent previous estimations of the He abundance at the edge of quiescent equatorial streamers during the minimum of cycle 22 (green line[14]), in the central region of equatorial streamers (blue line[14]) and inferred for the convection zone (red line[15]).

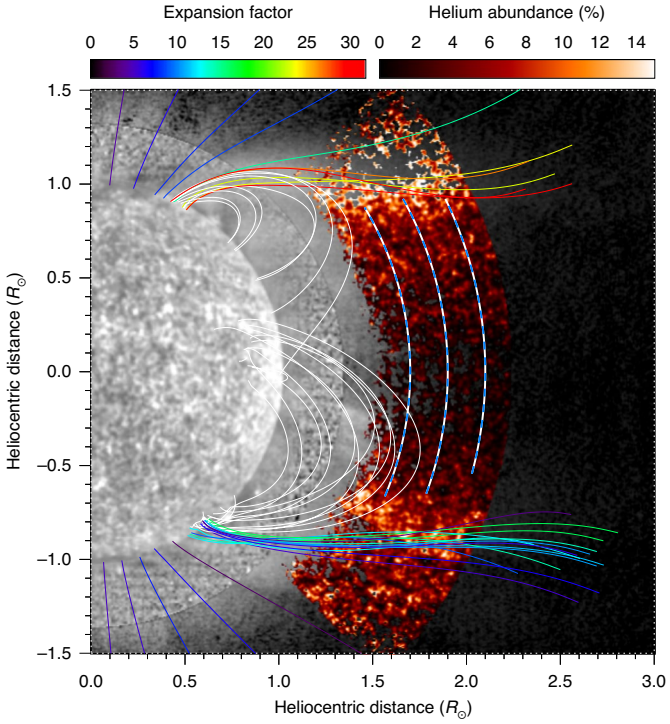

Fig. 3 | Magnetic topology of the solar corona in the region where the He abundance was measured. Extrapolated potential field lines are overlaid on the composite enhanced He II image of Fig. 1d (greyscale). The field lines are coloured according to the expansion factor (closed field lines are in white). The helium abundance is overplotted in red scale. The three blue dashed arcs mark the locations of the polar profiles in Fig. 2.

Sun–Earth Lagrangian point L1 with the Wind spacecraft in 2009, during the solar minimum of cycle 23. The wind He abundances measured at L1 reached anomalously low values, within 3.5% for wind flowing at 560 km s^{-1}, and less than 0.5% for the slowest wind flowing at 260 km s^{-1} (ref. [17]).

The exceptionally low speed of the solar wind observed at L1 originated in the equatorial region where the magnetic neutral line of the source surface field at 2.5$R_{\odot}$ is located, according to the photospheric magnetic field data obtained at the Wilcox Solar Observatory. The neutral line extends outward in the heliospheric current sheet where marked minima in the He abundance are typically measured[18]. The open field lines emerging from the equatorial region, although not evident in the extrapolation shown in Fig. 3, are likely to exist owing to the double or complex structure of the closed field line region. They outline the heliospheric current sheet further out and guide the very slow wind flowing in its proximity. The onset of the slow wind in the streamer core was measured directly by Doppler dimming[19]. The nascent solar wind was propagating along field lines, separating sub-streamers, in flux tubes characterized first by rapid expansion and subsequently by a narrowing of their cross-section before the wind reached the critical point, where the flow becomes supersonic . The depletion of oxygen observed with UVCS in the streamer cores has been attributed to this peculiar magnetic topology that has the effect of decreasing the wind speed in the corona without affecting the density[13]. A speed reduction results in a reduced proton flux and, as a consequence, a depletion of the oxygen ions. Therefore, by the same reasoning, we suggest that as the wind flowed along the flux tubes emerging from the core of the streamer belt, and having this particular topology, it slowed down in such a way as to influence locally the Coulomb drag; that is, the collisional coupling between helium ions and protons. This means that the reduced proton flux dragged a reduced number of helium ions in the solar wind[20,21], producing the low He abundance observed both in corona and in the heliosphere. The combination of this magnetic topology effect with the unusually slow wind conditions observed at L1 in 2009 resulted in a much greater helium depletion in interplanetary space than was measured during previous solar minima.

A similar geometry of the open field lines can be found in the regions immediately surrounding the boundaries between streamers and coronal holes[22,23], and it induces the same effect to slow down the local wind[24]. Moving away from the boundary, the flux tube divergence becomes monotonic and the wind speed increases

with distance from the streamer boundary as the flux tube expansion factor decreases. Therefore, we expect a consequent increase in the coronal He abundance with heliolatitude. Indeed, this effect is observed in the latitudinal profiles of Fig. 2 and in the coronal image of Fig. 3, which shows that along the open field lines surrounding the boundaries of the streamer belt, the He abundance increases with distance from the regions where the magnetic field is closed.

A strong helium depletion is also observed in the closed field regions in which the plasma is mainly confined (Fig. 3). However, in this case, it is likely that the low abundance arises from physical processes that are different from inefficient Coulomb drag; for example, gravitational settling in the plasma confined to closed magnetic field regions[25] or other processes that act to determine the elemental composition in the corona, such as wave–particle interaction[26,27].

The global images of He II in the solar atmosphere out to $3R_{\odot}$ demonstrate that the He abundance in the corona is modulated by the topology of the magnetic field lines and, from the very low values attained in the equatorial region, peaks at the boundaries between the quiescent streamers and the polar coronal holes where the solar wind speed is expected to increase. The extremely low coronal abundance of helium ions in the solar equatorial region caused the anomalously low helium abundance measured in the heliosphere during the minimum of activity in cycle 23.

Methods

Background. The first direct measure of the helium abundance in the corona was obtained with the Coronal Helium Abundance Experiment (CHASE) experiment on board Spacelab 2 (ref. [28]). The value derived at $1.15R_{\odot}$ was 7.9%, consistent with the photospheric values[3]. Unfortunately, these measurements were strongly affected by a stray-light background level that was larger than expected. More recently, an upper limit of 4.8% for the coronal helium abundance in quiescent streamers was determined from SOHO UVCS observations of the 108.5 nm He II Balmer line at $1.5R_{\odot}$ (ref. [14]). Similar observations of the He II Balmer line with the Solar Ultraviolet Measurements of Emitted Radiation instrument on board SOHO yielded a value of 5% (ref. [29]). Although the spread in He abundances in part can be attributed to the inherent uncertainties in the measurements, it can also be caused by the existence of temporal and spatial variations. For example, oxygen, another element with a high first ionization potential, has been shown to be depleted in the core of streamers[30]. Considering this possibility, and the variations of the wind elemental composition that depends on the flow speed observed in situ, we developed a suite of imaging coronagraphs to obtain a global map of the coronal helium abundance in the acceleration region of the solar wind, instead of performing localized spectroscopic measurements.

HERSCHEL combines, extends and refines the capabilities of the successful SOHO EIT, LASCO and UVCS instruments[31–33]. SCORE uses the same telescope optics for each wavelength and is the prototype for the Solar Orbiter Metis instrument[34–36]. HeCOR served as a prototype for the Full Sun Imager on board Solar Orbiter[37,38].

HERSCHEL calibration. A collimator capable of projecting a parallel beam of light in the visible, in the ultraviolet (120 nm) and two band passes in the extreme ultraviolet (17 nm and 30 nm) was assembled from Naval Research Laboratory test equipment used in the Skylab, SOHO and STEREO orbital missions (see ref. [39] for a description of a prototype). The light output of this collimator was calibrated using NIST-traceable photodiodes from International Radiation Detectors. This test set-up was used to characterize the stray-light performance of both coronagraphs and to achieve a good end-to-end throughput calibration of HECOR and the SCORE visible light and He II channels. The laboratory end-to-end throughput calibration of the SCORE H I channel was not fully successful, so the throughput projection that was constructed from component calibrations was validated by the SOHO UVCS H I Lyα measurement made in the co-ordinated joint observation programme for the HERSCHEL flight. The relevant absolute calibrations are: HECOR = 5.9×10^{9} ph cm^{-2} sr^{-1} DN^{-1} px^{-1}, SCORE H I = 4.3×10^{8} ph cm^{-2} sr^{-1} DN^{-1} px^{-1} and SCORE He II = 8.4×10^{8} ph cm^{-2} sr^{-1} DN^{-1} px^{-1}.

Observations from each of the HERSCHEL instruments were compromised by in-flight anomalies. The thin aluminium filter that blocked visible light from the HECOR detector developed a pinhole. The impact of this HECOR anomaly was minimized in the post-flight image analysis. The optical alignment of SCORE moved during launch, which resulted in a relative misalignment of the external and internal occulters. The impact of the SCORE anomaly was a total loss of the visible light channel. In the SCORE H I (ultraviolet) and He II (extreme ultraviolet) channels, the image of the east half (in heliocentric coordinates) of the corona was lost, but the west half was largely unaffected.

He abundance derivation. The helium abundance was deduced from the H I and He II line intensity ratio. The intensity of the resonantly scattered H and He lines can be expressed as

$$I_{\rm ion} = hB_{12}^{\rm ion}\int_0^{\infty} n_{\rm ion}\int_{\Omega} p(\theta)I_{\odot}f\left(v_{\rm ion},T_{\rm ion},P_{\odot,{\rm ion}}\right){\rm d}\Omega{\rm d}s$$

where h is the Planck constant, $B_{12}^{\rm ion}$ is the Einstein coefficient for absorption, $n_{\rm ion}$ is the ion number density, $p(\theta)$ accounts for the anisotropy of the scattering, $I_{\odot}$ is the total intensity of the chromospheric exciting line and $f\left(v_{\rm ion},T_{\rm ion},P_{\odot,{\rm ion}}\right)$ is a function of the ion velocity, temperature and chromospheric profile. In the case of the H I line emission, the chromospheric photons are scattered by neutral hydrogen atoms. According to images obtained with the SOHO LASCO C2 and C3 coronagraphs in the days immediately preceding and following the rocket launch, the corona showed persistent features at latitudes above and below the equator indicative of a roughly cylindrical symmetry. Therefore, we assumed that the observed emission primarily comes from the plane of the sky. Hence, the line intensity ratio can be expressed as

$$\frac{I_{\rm He}}{I_{\rm H}} = A_{\rm He}\frac{N_{\rm He^{+}}/N_{\rm He}}{N_{\rm H^{0}}/N_{\rm H}}\frac{B_{12}^{\rm He}}{B_{12}^{\rm H}}\frac{I_{\odot{\rm He}}}{I_{\odot{\rm H}}}\frac{f\left(v_{\rm He},T_{\rm He},P_{\odot,{\rm He}}\right)}{f\left(v_{\rm H},T_{\rm H},P_{\odot,{\rm H}}\right)}$$

Ionization balance and transition rates are taken from refs. [40–42]. Contribution functions are given by the product of the ionization equilibrium R_i and the collisional excitation rate coefficient of the atomic transition C_{12}. The contribution functions of the H I 121.6 nm and He II 30.4 nm lines calculated using the atomic parameters adopted in our analysis were compared to those derived using parameters from the CHIANTI atomic database[43], and showed no significant differences. The intensity profile of the on-disk H I Lyα 121.6 nm spectral line has been derived[44]. This full Sun Lyα intensity profile has been scaled to the 121.6 nm irradiance on 14 September 2009, as provided by the SOlar Stellar Irradiance Comparison Experiment (SOLSTICE) on board the SOlar Radiation and Climate Experiment (SORCE) spacecraft: $I_{ex,121.6} = 5.323\times10^{15}$ ph cm^{-2} s^{-1} sr^{-1}. The He II disk profile was assumed to be a Gaussian with a full-width at half-maximum of 0.01 nm (for example, refs. [45,46]). This profile has been scaled to the solar irradiance $I_{ex,30.4} = 1.390\times10^{14}$ ph cm^{-2} s^{-1} sr^{-1}, which was determined from the SORCE SOLSTICE Lyα irradiance using the empirical relationship in ref. [47]. Considering the lack of active regions on the solar surface at the time of flight, we assumed a constant intensity and shape for the chromospheric H and He II profiles across the solar disk. The coronal H absorbing profiles were derived from the neutral hydrogen kinetic temperature given in ref. [48], and the same value was used for the He ion kinetic temperature.

To derive the helium abundance from the He II and H I line intensity ratio, it is necessary to determine the contributions to the He II emission of other lines falling in the SCORE imaging telescope passband, which is approximately 1 nm wide and determined by its multi-layer coating and filter. In particular, emission from the Si XI 30.3 nm line makes an important contribution wherever there is a 1.5 MK plasma along the line of sight.

The approach adopted to remove the Si XI intensity contamination does not require information about the electron temperature of the coronal plasma. The intensity measured in the He channel of SCORE is primarily composed of two contributions. One component, which is dominant at lower coronal heights, is due to the Si XI 30.3 nm emission produced by collisions of the silicon ions with free electrons, which decreases with heliodistance as n_e^2. At higher heights, the dominant contribution is due to the He II 30.4 nm line, which is formed by resonant scattering of the disk radiation by coronal helium ions and decreases as n_e. The height at which the Si XI line becomes negligible is marked clearly in the data by a change of slope; that is, a well-defined knee is present in the radial profile of the observed $I_{\rm He,SCORE}$. It can be proved that the Si XI contribution is indeed negligible above the knee by computing the ratio of the coronal polarized brightness, pB, a quantity proportional to electron density, and the intensity measured in the SCORE He channel. Above the knee, this curve is essentially flat as a function of height, which implies that both quantities are proportional to electron density; hence, the signal in the He channel at coronal heights above the knee is due entirely to the He II 30.4 nm emission by resonance scattering. The pB value was obtained from the data obtained with the Mark IV K-coronagraph at the High Altitude Observatory at Mauna Loa Solar Observatory on 15 September 2009.

The He channel intensity measured above the knee was fitted with a combination of two power laws, and then the fit was extrapolated down to the inner limit of the SCORE field of view. As the curve obtained in this way is representative of the radial profile of the He II line intensity, the Si XI contribution at lower heights can be isolated and removed accurately.

However, the electron temperature T_e is needed to estimate the coronal helium abundance, and it can be derived by comparing the SCORE observations with a model corona for the H I and He II line emission that is valid at the minimum of solar activity. The coronal electron density profile determined using the van de Hulst inversion of the pB value measured with the Mark IV K-coronagraph between 1.14 and $2.86R_{\odot}$, and that measured with SOHO LASCO C2 above $2R_{\odot}$, is similar to the density profile in ref. [49]. For this reason, the hydrostatic T_e profile

deduced in ref. [49] from the ideal gas law was adopted for the H I and He II line intensity calculations.

To take into account the fact that the coronal He abundance was measured with SCORE in September 2009, during the deepest, long-lasting solar activity minimum of the space era, and when freeze-in coronal temperatures (namely, temperatures at the coronal source regions of the wind streams) inferred from charge-state ratios in the heliosphere were anomalously low[17], we have derived the coronal He abundance from the ratio of the He and H line intensities in two ways. In the first calculation, we assumed typical coronal temperatures of a quiescent streamer during a solar minimum (for example, in ref. [49]). In the second calculation, we decreased these temperatures by the maximum drop (20%) found in the freeze-in temperatures[17] that can be reasonably ascribed to a low-latitude (close to the equator) coronal region, which may have been the source of the solar wind measured in situ at L1. However, the difference between the abundances derived by these two methods was well within the errors estimated for the abundance and shown in Fig. 2. In the latitude range across the solar equator considered in the analysis, the expansion speed of the corona is less than 70 km s^{-1}, as inferred by the application of Doppler dimming techniques[16,50] to the SCORE H I data. Therefore, the coronal dynamics affects the He abundance results only marginally. Analyses of the co-ordinated SOHO UVCS observations of O VI are consistent with the expansion rate derived for the hydrogen observations.

Comparison with context data. Figure 1d is a composite of HECOR observations and those obtained simultaneously by SOHO EIT. At the edge of the EIT field of view there is a significant background created by light scattered from the bright solar disk by the first-generation multi-layer optics used in EIT. Therefore, to make a useful comparison between EIT and HECOR, it is important to correct the EIT image by de-convolution, using the point-spread function as described in refs. [51,52]. Co-alignment of the images was achieved using pointing information only; that is, without a priori assumptions about the identity of the structures observed by the two instruments to obtain an alignment by cross-correlation. There is a very good correspondence between structures observed in the outer part of the EIT field and in the inner part of the HECORE field. The alignment is particularly clear at the edges of the streamers. We also note that plumes observed with EIT above the solar north pole continue out to about 1.7$R_{\odot}$ in the HECOR field of view. This agreement between the HECOR and EIT data is expected because the two instruments have very similar passbands.

The field of view in Fig. 1d is extended beyond that of HECOR with the image obtained by the SOHO LASCO C2 visible light coronagraph. The correspondence between features observed by HECOR and C2 (as well as in the SCORE He II and LASCO data) is visibly poorer than that between HECOR and EIT. The plumes observed by HECOR extend into the field of C2, but there are plumes visible in the C2 image above the north pole with no counterpart in the HECOR image. This may be due, at least in part, to the low signal-to-noise ratio of the HECOR data over the poles. Visible extensions of the streamers above the western boundary in the HECOR and SCORE He II images align with the brightest parts of streamers in the C2 image. However, the detailed structure within each streamer is very different in the HERSCHEL He II and visible light images. Furthermore, emission depletion in the region between streamers is much more pronounced in HECOR and SCORE He II observations than in the C2 visible light data.

The C2 coronagraph observes Thomson scattering of visible light photospheric radiation by free electrons in the corona. The intensity measured by C2 is proportional to the integral of the electron density along the line of sight. However, the intensity measured by HECOR is the integral over the line of sight of a function that depends not only on the electron density, but also on several other parameters, including the temperature of the helium ions and their abundance. Therefore, any differences between the HECOR and C2 images indicate that the coronal intensity variations observed by HECOR are not due entirely to changes in total coronal density.

Data availability

The imaging data that support the plots within this paper and other findings of this study are available from the NASA Goddard Coordinated Data Analysis Workshop (CDAW) Data Center (https://cdaw.gsfc.nasa.gov/) or from the corresponding author on reasonable request. The data from Fig. 2 are provided as Source data files.

Code availability

All relevant codes used during this study are available from the corresponding author on reasonable request. Source data are provided with this paper.

Received: 6 November 2019; Accepted: 23 June 2020;
Published online: 27 July 2020

References

1. Christensen-Dalsgaard, J. The 'standard' Sun. *Space Sci. Rev.* **85**, 19–36 (1998).
2. Kosovichev, A. G. et al. Sources of uncertainty in direct seismological measurements of the solar helium abundance. *Mon. Not. R. Astron. Soc.* **259**, 536–558 (1992).
3. Gabriel, A. H. et al. SpaceLab 2 measurement of the solar coronal helium abundance. *Adv. Space Res.* **15**, 63–67 (1995).
4. Feldman, U. FIP effect in the solar upper atmosphere: spectroscopic results. *Adv. Space Res.* **85**, 227–240 (1998).
5. Buergi, A. Proton and alpha particle fluxes in the solar wind: results of a three-fluid model. *J. Geophys. Res.* **97**, 3137–3150 (1992).
6. Aellig, M. R., Lazarus, A. J. & Steinberg, J. T. The solar wind helium abundance: variation with wind speed and the solar cycle. *Geophys. Res. Lett.* **28**, 2767–2770 (2001).
7. Hansteen, V. & Velli, M. Solar wind models from the chromosphere to 1 AU. *Space Sci. Rev.* **172**, 89–121 (2012).
8. Fineschi, S. et al. Ultraviolet and visible-light coronagraphic imager (UVCI) for HERSCHEL (Helium Resonance Scattering in Corona & HELiosphere). *Proc. SPIE* **4853**, 162–171 (2003).
9. Romoli, M. et al. The HERSCHEL/SCORE visible and UV coronagraph. In *Proc. Second Solar Orbiter Workshop* SP-641 (eds Marsch, E. et al.) 79 (ESA, 2007).
10. Auchère, F. et al. HECOR: HElium CORonagraphy aboard the Herschel sounding rocket. *Proc. SPIE* **6689**, https://doi.org/10.1117/12.751447 (2007).
11. Howard, R. A. et al. Sun Earth Connection Coronal and Heliospheric Investigation (SECCHI). *Space Sci. Rev.* **136**, 67 (2008).
12. Schwenn, R. et al. First view of the extended green-line emission corona at solar activity minimum using the Lasco-C1 coronagraph on SOHO. *Sol. Phys.* **175**, 667–684 (1997).
13. Noci, G. et al. The quiescent corona and slow solar wind. In *Proc. Fifth SOHO Workshop* SP-404 (ed. Wilson, A.) 75–84 (ESA, 1997).
14. Raymond, J. C. et al. Composition of coronal streamers from the SOHO ultraviolet coronagraph spectrometer. *Sol. Phys.* **175**, 645–665 (1997).
15. Grevesse, N. & Sauval, A. J. Standard solar composition. *Space Sci. Rev.* **85**, 161–174 (1998).
16. Withbroe, G. L. et al. Probing the solar wind acceleration region using spectroscopic techniques. *Space Sci. Rev.* **33**, 17–52 (1982).
17. Kasper, J. C. et al. Evolution of the relationships between helium abundance, minor ion charge state, and solar wind speed over the solar cycle. *Astrophys. J.* **745**, 162–168 (2012).
18. Borrini, G. et al. Solar wind helium and hydrogen structure near the heliospheric current sheet - a signal of coronal streamers at 1 AU. *J. Geophys. Res.* **86**, 4565–4573 (1981).
19. Noci, G. & Gavryuseva, E. Plasma outflows in coronal streamers. *Astrophys. J.* **658**, L63–L66 (2007).
20. Geiss, J., Hirt, P. & Leutwyler, H. On acceleration and motion of ions in corona and solar wind. *Sol. Phys.* **12**, 458–483 (1970).
21. Wang, Y.-M. Relating the solar wind helium abundance to the coronal magnetic field. *Astrophys. J.* **683**, 499–509 (2008).
22. Wang, Y.-M. & Sheeley, N. R. Jr. Solar wind speed and coronal flux-tube expansion. *Astrophys. J.* **355**, 726–732 (1990).
23. Antonucci, E. Wind in the solar corona: Dynamics and composition. *Space Sci. Rev.* **124**, 35–50 (2006).
24. Antonucci, E., Abbo, L. & Telloni, D. UVCS observations of temperature and velocity profiles in coronal holes. *Space Sci. Rev.* **172**, 5–22 (2012).
25. Li, J. Physical structure of a coronal streamer on the closed-field region as observed from UVCS/SOHO and SXT/Yohkoh. *Astrophys. J.* **506**, 431–438 (1998).
26. Rakowski, C. E. & Laming, J. M. On the origin of the slow speed solar wind: helium abundance variations. *Astrophys. J.* **754**, 65–75 (2012).
27. Laming, J. M. Non-WKB models of the FIP effect: the role of slow-mode waves. *Astrophys. J.* **744**, 115–128 (2012).
28. Patchett, B. et al. The coronal helium abundance experiment on Spacelab 2. *Space Sci. Rev.* **29**, 431–437 (1981).
29. Laming, J. M. & Feldman, U. The solar helium abundance in the outer corona determined from observations with SUMER/SOHO. *Astrophys. J.* **546**, 552–558 (2003).
30. Kohl, J. L. et al. First results from the SOHO ultraviolet coronagraph spectrometer. *Sol. Phys.* **175**, 613–644 (1997).
31. Delaboudinière, J. -P. et al. EIT: Extreme-ultraviolet imaging telescope for the SOHO mission. *Sol. Phys.* **162**, 291–312 (1995).
32. Brueckner, G. E. et al. The large angle spectroscopic coronagraph (LASCO). *Sol. Phys.* **162**, 357–402 (1995).
33. Kohl, J. L. et al. The ultraviolet coronagraph spectrometer for the Solar and Heliospheric Observatory. *Sol. Phys.* **162**, 313–356 (1995).
34. Fineschi, S. et al. METIS: a novel coronagraph design for the Solar Orbiter mission. *Proc. SPIE* **8443**, 84433H–1 (2012).
35. Fineschi, S. et al. Optical design of the multi-wavelength imaging coronagraph Metis for the Solar Orbiter mission. *Exp. Astron.* **49**, 239–263 (2020).
36. Antonucci, E. et al. Metis: The Solar Orbiter visible light and ultraviolet coronal imager. *Astron. Astrophys.* (in the press).
37. Auchère, F. et al. Innovative designs for the imaging suite on Solar Orbiter. *Proc. SPIE* **5901**, 590115 (2005).
38. Rochus, P. et al. The extreme ultraviolet imager on Solar Orbiter. *Astron. Astrophys.* (in the press).

39. Defise, J. M. *Analyse des performances instrumentales du téléscope spatial EIT*. PhD thesis, Université de Liège (1999).
40. Arnaud, M. & Rothenflug, R. An updated evaluation of recombination and ionization rates. *Astron. Astrophy. Suppl. Ser.* **60**, 425–457 (1985).
41. Elwert, G. Über die Ionisations- und Rekombinationsprozesse in einem Plasma und die Ionisationsformel der Sonnenkorona. *Z. Naturforsch.* **7**, 432–439 (1952).
42. Gabriel, A. H. & Jordan, C. in *Case Studies in Atomic Collision Physics* 1st edn, Vol. 2 (eds McDaniel, E. W. & McDowell, M. R. C.) Ch. 4 (North-Holland, 1972).
43. Dere, K. P. et al. CHIANTI - an atomic database for emission lines. IX. Ionization rates, recombination rates, ionization equilibria for the elements hydrogen through zinc and updated atomic data. *Astron. Astrophys.* **498**, 915–929 (2009).
44. Lemaire, P. et al. Variation of the full Sun hydrogen Lyman profiles through solar cycle 23. *Adv. Space Res.* **35**, 384–387 (2005).
45. Doschek, G. A., Behring, W. E. & Feldman, U. The widths of the solar He I and He II lines at 584, 537, and 304 Å. *Astrophys. J.* **190**, L141–L142 (1974).
46. Brosius, J. W. Measuring active and quiet-sun coronal plasma properties with extreme-ultraviolet spectra from SERTS. *Astrophys. J. Suppl.* **106**, 143–164 (1996).
47. Auchère., F. Effect of the H I Lyα chromospheric flux anisotropy on the total intensity of the resonantly scattered coronal radiation. *Astrophys. J.* **622**, 737–743 (2005).
48. Antonucci, E., Abbo, L. & Dodero, M. A. Slow wind and magnetic topology in the solar minimum corona in 1996-1997. *Astron. Astrophys.* **435**, 699–711 (2005).
49. Gibson, S. et al. Solar minimum streamer densities and temperatures using Whole Sun Month coordinated data sets. *J. Geophys. Res.* **104**, 9691–9700 (1999).
50. Noci, G., Kohl, J. L. & Withbroe, G. L. Solar wind diagnostics from Doppler-enhanced scattering. *Astrophys. J.* **315**, 706–715 (1987).
51. Auchère, F. & Artzner, G. E. EIT observations of the 15 November 1999 Mercury transit. *Sol. Phys.* **219**, 217–230 (2004).
52. Auchère, F. *An observational study of helium in the solar corona with the EIT instrument on board the SOHO spacecraft*. PhD thesis, Université Paris VI (2000).

Acknowledgements

The HERSCHEL suborbital investigation was funded by the NASA Heliophysics Living With a Star Program. The SCORE coronagraph (principal investigator, E.A.) was funded by the Ministero dell'Istruzione, dell'Università e della Ricerca (MIUR) under grant COFIN 2002, the Italian Space Agency (ASI) under grant ASI-I/015/07/0 and the Osservatorio Astrofisico di Torino of the Istituto Nazionale di Astrofisica (INAF). The HECOR coronagraph (principal investigator, F.A.) was developed at IAS and funded by Centre National d'Etudes Spatiales (CNES). The magnetic field extrapolations were performed using models that are part of the SolarModels facilities. SolarModels is supported by CNES. J.M.L. and D.W. were supported by NASA Heliophysics Supporting Research (NNH16AC39I), Heliophysics Grand Challenges (NNH17AE96I), Heliophysics Guest Investigators (80HQTR19T0029) and by basic research funds of the CNR. The HERSCHEL team would like to express their extreme gratitude to Dave Roberts, who, although he is no longer with us, continues to inspire by his example and dedication to the many missions he helped over the course of his long career. E.A. would also like to acknowledge A. Gherardi, L. Gori, G. Noci, E. Pace, D. Paganini, D. Gardiol, D. Loreggia, V. Da Deppo, M. G. Pelizzo, G. Naletto, P. Nicolosi and G. Tondello for their contributions to the development of SCORE.

Author contributions

All authors contributed to the proposal and planning of observations, the data interpretation and the writing of the manuscript. J.D.M. is principal investigator of the HERSCHEL sounding rocket. E.A. is co-principal investigator and led the development of SCORE with assistance from S.F., M.R., G.M., M.F., F.L., A.M.M., M.P. and L.Z. F.A. led the development of HECOR with assistance from F.R., J.-P.M. and J.-C.L. J.S.N. was HERSCHEL project scientist and led the development of HEIT with assistance from J.L., J.-P.W. and D.W. D.T. developed the codes for the analysis of the SCORE data and for the cross-checking with the UVCS data. G.R., L.A., J.M.L., N.B., C.G. and A.C. assisted in analysing data. J.L.K. and L.D.G. performed the UVCS observations.

Competing interests

The authors declare no competing interests.

Additional information

Supplementary information is available for this paper at https://doi.org/10.1038/s41550-020-1156-6.

Correspondence and requests for materials should be addressed to J.D.M. or J.N.

Reprints and permissions information is available at www.nature.com/reprints.

Publisher's note Springer Nature remains neutral with regard to jurisdictional claims in published maps and institutional affiliations.